Materials Advances

PAPER

Check for updates

Methane conversion and hydrogen production over TiO₂/WO₃/Pt heterojunction photocatalysts†

Saulo Amaral Carminati, [*a] Eliane Ribeiro Januário, [a]
Arthur Pignataro Machado, [b] Patrícia Ferreira Silvaino, [a] Jorge Moreira Vaz [a] and
Estevam Vitorio Spinacé [*a]

Along with the advantages of mild reaction conditions, simple operation, and low energy consumption, the photocatalytic conversion of methane in the presence of water presents great potential in facilitating direct methane conversion into value-added chemicals and H_2 generation. In this work, TiO_2/WO_3 heterojunction photocatalysts modified with Pt nanoparticles were synthesized and their performances towards methane conversion into ethane (C_2H_6) and hydrogen (H_2) in the presence of water were evaluated. The ternary photocatalysts were characterized by X-ray diffraction, UV-vis, scanning and transmission electron microscopy and X-ray photoelectron spectroscopy. The highly active $TiO_2/WO_3/Pt$ photocatalyst achieved C_2H_6 and H_2 production rates of 1.18 mmol g^{-1} h^{-1} and 57 mmol g^{-1} h^{-1}, respectively. These values were 37% (for C_2H_6) and 34% (for H_2) higher than those produced by a $TiO_2/$ Pt photocatalyst. The results show that the presence of WO_3 in a very small concentration on TiO_2 with the introduction of Pt as a co-catalyst contributes to achieving higher activities towards both C_2H_6 and H_2 evolution.

Introduction

It is common sense that the rise in global population increases the demand for energy, which is mainly met by fossil resources, like coal, natural gas or oil.[1] The consumption of fossil fuels and the emission of CO_2 and other greenhouse gases have increased since the pre-industrial era, presenting one of the most pressing world challenges. The scientific and industrial community efforts over the last few decades have been spurred towards developing CO_2-free emission technologies.[2,3]

Methane (CH_4), a potent greenhouse gas and a ubiquitous natural carbon resource, has been mainly used as an energy supply. It has the most robust C–H bonds (439 kJ mol^{-1}) with the highest activation barrier among hydrocarbon molecules,[4] requiring high temperatures and pressures to achieve high conversion rates, thereby making its conversion more challenging.[5] Only about 10% of methane is utilized for chemical production to synthesize a variety of high-value-added chemicals.[6] In this sense, the catalytic conversion of CH_4 into multicarbon (C_{2+}) products under mild conditions has received

worldwide attention in the last few years.[7] While many approaches have been followed over the years,[8] photocatalysis is a promising game-changer. Employing solar energy would be one of the possible alternatives to overcome drawbacks associated with the thermodynamic barrier for the direct conversion of methane under mild conditions.[9,10]

Photocatalytic dehydrogenative coupling of methane in the presence of water has been recently reported in gas, liquid and gas–liquid–solid systems.[11] Here, photocatalytic water splitting into H_2 and methane conversion to the more valuable product C_2H_6 (ethane) are involved in the same reaction system, where CH_4 is the sacrificial agent for holes.[12] Ishimaru and co-workers[13] investigated the effect of adding water vapor on the C_2H_6 formation rate over a Pd/Ga_2O_3 photocatalyst during CH_4 conversion and the results showed that water promoted a substantial improvement in the C_2H_6 (selectivity > 80%) and H_2 production (AQE = 14.4%). Despite progress, additional efforts must be done to bridge the gap between experimental studies and industrial implementation, which remains extremely challenging.[14]

Many kinds of semiconductor-based photocatalysts, such as TiO_2,[15] GaN,[16,17] Ga_2O_3,[18,19] $BiVO_4$[20] and ZnO,[21] have been developed for various types of methane conversion, including direct and indirect routes, tuning the product selectivity. The CH_4 conversion and the selectivity of C_2H_6 are both low on pristine TiO_2 due to poor separation efficiency of the photogenerated carriers, resulting in the production of undesired but

*a Instituto de Pesquisas Energéticas e Nucleares, IPEN-CNEN/SP,
Av. Prof. Lineu Prestes, 2242-Cidade Universitaria, São Paulo, 05508-000, Brazil.
E-mail: saulocarminati89@gmail.com, espinace@ipen.br
*b Laboratório de Nanotecnologia e Energia Solar, Instituto de Química,
Universidade Estadual de Campinas, Campinas, 13083-970, SP, Brazil

thermodynamically favorable overoxidized products (*i.e.*, CO and CO_2).[14]

Among many semiconductors, it is well known that commercial TiO_2 (P25) is taken as a proof-of-concept model for direct conversion of methane (CH_4) toward value-added multi-carbon (C2 +) compounds,[22] either through non-oxidative[23] or oxidative routes.[24] To overcome the poor performance of TiO_2 under visible light and high recombination rate of the charge carriers, strategies like ion doping and heterojunction construction have shown great results in photocatalysis.[25] In particular, heterojunction systems have been attempted as an effective strategy for enhancing the overall photocatalytic efficiency of TiO_2-based photocatalysts.[26] For heterojunctions, the incorporation of alternative semiconductors such as WO_3 may synergistically improve the photocatalytic efficiency of TiO_2 under visible light irradiation, resulting from optical and electronic property modification.[27,28] Additionally, the use of various co-catalysts is proven to be an effective approach to augment charge carrier separation.[29]

In this work, we investigated the photocatalytic properties of TiO_2/WO_3 heterojunction photocatalysts towards methane conversion into ethane (C_2H_6) and hydrogen in the presence of water through a gas–solid–liquid photocatalytic reaction system. To either promote better charge separation and more active sites for H_2 production, Pt nanoparticles were deposited over the heterojunction photocatalyst surface. This work takes a step forward and presents for the first time the study of C_2H_6 photogeneration from CH_4 conversion concomitantly with hydrogen evolution over photocatalysts based on TiO_2/WO_3 modified with Pt to increase the charge carrier separation under mild conditions. Different concentrations of WO_3 were utilized and the photocatalytic activities were evaluated.

Experimental and discussion

Materials and methods

Titanium(IV) dioxide P25 (Degussa) was used as the support material. Ammonium tungstate hydrate $((NH_4)_{10}(H_2W_{12}O_{42})\cdot 4H_2O)$, ethanol ($C_2H_6O$), isopropyl alcohol ($C_3H_8O$), nitric acid ($HNO_3$), ethylene glycol ($C_2H_6O_2$), and chloroplatinic acid ($H_2PtCl_6\cdot 6H_2O$) were used. Deionized water used in the experiments was purified to 18.2 MΩ cm resistivity using an ultra-pure Milli-Q Millipore system.

Sample preparation

Synthesis of $TiO_2/WO_3/Pt$ photocatalysts. Firstly, the monoclinic phase of WO_3 was obtained by dissolving 2 g of ammonium tungstate hydrate $((NH_4)_{10}(H_2W_{12}O_{42})\cdot 4H_2O)$ in 85 mL of deionized water at 80 °C. Subsequently, 15 mL of concentrated HNO_3 was added dropwise, and the suspension was kept stirring for 30 min under constant reflux. The suspension was then transferred to an ultrasonic bath for 30 min. The resulting material was filtered, washed with deionized water, and dried at 80 °C for 24 h. The obtained powder was ground and calcined at 500 °C (ramp rate of 10 °C min^{-1}) for 4 h in air.

For the synthesis of $TiO_2/WO_3/Pt$, a proper amount of TiO_2 (P25 Degussa) was added into a 250 mL round-bottom flask containing 250 mL of ethylene glycol/water 3 : 1 v/v solution. The suspension was stirred for 10 min and then sonicated for another 10 min. A desired aliquot of $H_2PtCl_6\cdot 6H_2O$ aqueous solution and a proper amount of the as-synthesized WO_3 were added dropwise with continuous stirring until complete homogenization, to obtain 500 mg of material varying the WO_3 concentration (0.1, 1, 3, 6, 12 and 25%). The Pt concentration was set to 0.5%, as it was the best amount of Pt previously tested by the group. The system was stirred under reflux at 180 °C for 1 h and then, the material was washed, centrifuged and dried at 80 °C for 2 h.

Photocatalytic activity. The photocatalytic activity of the photocatalysts was evaluated in a gas–liquid–solid system, described in our previous works.[19,21] In a typical procedure, 75 mg of the photocatalyst was dispersed in 250 mL of ultra-pure water (18.2 MΩ cm @ 25 °C) in a commercial 250 mL Ace reactor. A steady stream of CH_4 (under 25 mL min^{-1} of flow rate, controlled with a mass flow controller) was constantly circulated through the suspension during the reaction, whereas a 450 W Hg lamp (UVA/B/C) was used as a light source. In order to maintain the reaction (~60 °C) and the Hg lamp (~40 °C) temperatures, a water circulation system was used. The amount of the main evolved products (CO_2, C_2H_6, C_3H_8, CO and H_2) was quantified with gas chromatography-mass spectrometry (GC-MS) equipment (Agilent 7890B coupled to MSD 5977B). The equipment has a thermal conductivity detector (TCD), methanizer (MET), and flame ionization detector (FID), as well as a quadrupole mass spectrometer detector (MSD) and two capillary columns (plot U and a molecular sieve 5 Å column). The product selectivity was calculated by the following equation:

$$\text{Carbon product selectivity (\%)} = \frac{C\ \text{product}}{C_2H_6 + C_3H_8 + CO + CO_2}$$

(1)

Characterization of the materials

The crystalline structure of the materials was analyzed by X-ray diffraction (XRD) using Cu Kα radiation ($\lambda = 0.15418$ nm) and the XRD patterns were recorded on a Rigaku Miniflex II apparatus, with scanning at 2θ from 20° to 90° with 0.05 step and 2 s count. The UV-Vis diffuse reflectance spectra were recorded using a UV-Visible spectrophotometer with a wavelength range of 200–800 nm. The Pt content (wt%) was determined by wavelength-dispersive X-ray fluorescence (WD-XRF) spectroscopy on Rigaku Supermini equipment (Pd source, 50 kV–4 mA) using a calibration curve. The morphology of the photocatalysts was evaluated by transmission electron microscopy (TEM) at an acceleration voltage of 200 kV and the images were collected on a JEOL equipment model JEM 2100F. A scanning electron microscope (SEM) equipped with an energy dispersive X-ray spectroscopy (EDX) unit was used for elemental mapping. The valence states of each element were studied by X-ray photoelectron spectroscopy (XPS, Thermo

Fisher Scientific) with an Al Kα X ray source ($h\nu$ = 1486.6 eV). The photoluminescence (PL) spectra of the solid photocatalysts were taken with an Ocean Optics 2000 luminescence spectrometer + USB spectrometer with a CCD camera. The excitation wavelength was 265 nm and the spectra were recorded at room temperature over the range of 200–1000 nm, with the scanning speed at 1000 nm min^{-1}, and the PMT voltage was 650 V.

Results and discussion

Commercial TiO_2 (P25) comprises both anatase and rutile phases with an estimated composition of 84.2% anatase and 15.8% rutile.[10] The XRD patterns of TiO_2, WO_3 and $TiO_2/WO_3/Pt$ with 0.5 wt% of Pt varying the amount of WO_3 are displayed in Fig. 1a. Given the low Pt content of the samples, no peaks different from those found in the TiO_2 or TiO_2/WO_3 matrix were observed in the XRD patterns of the as-prepared photocatalysts. It can be observed that the anatase phase (JCPDS 00-021-1272, labelled ●) predominates in the crystalline structure of TiO_2 in all materials with a small rutile increment (labelled ★).[12] Upon WO_3 incorporation (labelled ∗), the peaks of the monoclinic phase type (JCPDS 00-043-1035) of WO_3 could be clearly seen only for TiO_2/WO_3 samples with 12% and 25%.[30] Since the materials were not further calcined, the anatase/rutile proportion remained the same, as indicated by the XRD patterns. The synthesized photocatalysts were also characterized by UV-vis diffuse reflectance spectroscopy (DRS), and the sample spectra are shown in Fig. 1b. It is possible to notice that the TiO_2 photocatalyst activation occurs around 400 nm of UV light. Upon WO_3 incorporation, by increasing the concentration of WO_3 in the composite, the reflectance tends to show a red shift, resulting from the combination of the two materials absorption with further contribution in the visible range of the small amount of Pt incorporated.

The optical band gap (E_g) of the as-prepared photocatalysts was determined by the Kubelka–Munk plots (ESI† (Fig. S1 and Table S1)). The E_g values of 3.10 and 2.68 eV agree with previous reports for TiO_2 (P25)[31,32] and WO_3,[33,34] respectively. The photocatalysts with a lower amount of WO_3 (1% and 3%) did

not change the E_g when compared with pristine TiO_2. The $TiO_2/WO_3/Pt$ photocatalysts with 6, 12 and 25% showed E_g values of 3.03, 3.02 and 2.93 eV, respectively, proving their capacity to additionally absorb parts of the visible light.

Fig. 2 shows the morphology of the as-prepared photocatalysts using TiO_2 (P25 Degussa) as the support material, characterized by TEM. In Fig. 2a, it can be seen that Pt nanoparticles have a spherical shape, with nanoparticle sizes in the range of 2–5 nm. Fig. 2b shows the TEM images of the TiO_2/WO_3 heterojunction photocatalyst, with 6% of WO_3. WO_3 exhibits an irregular shape with sizes in the range of 5–15 nm. Additionally, the WO_3 did not cover the entire surface of TiO_2, but was deposited randomly around its surface.

Fig. 2c–f depicts the $TiO_2/WO_3/Pt$ ternary composite morphology with the EDS mapping image, where WO_3 (0.1 wt%) and Pt nanoparticles seem to be more agglomerated. The element distributions confirm the presence of Ti, O, W and Pt under high magnification. The EDX spectrum of the $TiO_2/WO_3/Pt$ photocatalyst is shown in Fig. S2. The crystal structure information was further investigated by HRTEM. Fig. 2g–i show the morphology of the as-prepared $TiO_2/WO_3/Pt$ ternary composite.

It can be observed that Pt nanoparticles are well distributed throughout the material. The clear lattice fringes with the spacings of 0.35 nm, 0.23 nm and 0.39 nm in a high-resolution TEM (HRTEM) image can be assigned to the (101), (111) and (020) crystal planes of TiO_2, Pt and WO_3 nanoparticles, respectively.[35,36]

The XPS analysis was used to determine the surface composition and the chemical valence state of the elements in the as-prepared samples, as shown in Fig. 3a–d. The XPS survey spectrum of the ternary composite is shown in Fig. 3a, indicating the presence of Ti, O, W and Pt elements. The survey spectrum of pristine TiO_2 can be found in the ESI† (Fig. S3). In the Ti high-resolution spectrum (Fig. 3b), the peaks at 465.29 eV correspond to $Ti2p_{1/2}$ and 459.57 eV to $Ti2p_{3/2}$, respectively. Furthermore, the distance of the two peaks indicates the presence of Ti^{4+}.[37] The W4f (Fig. 3c) peaks split into two peaks at 36.26 eV ($W4f_{5/2}$) and 38.17 eV ($W4f_{7/2}$), indicating the presence of W^{6+}. The peaks at 74.78 eV and 71.42 eV (Fig. 3d) correspond to Pt 4f5/2 and Pt 4f7/2, respectively.[38] The peak shapes can be attributed to nanoparticles with Pt^0 chemical state. No different oxidation states of Pt were observed, indicating the total reduction of Pt^{4+} to Pt^0.

The effect of the improved charge separation by loading Pt nanoparticles on TiO_2/WO_3 in a heterojunction configuration could be evaluated by the photocatalytic methane conversion with simultaneous hydrogen evolution under UV illumination (75 mg of photocatalyst + 250 mL of ultrapure water, methane flow 25 mL min^{-1}). Fig. 4 shows the CO_2, C_2H_6 and H_2 evolution rates (μmol g^{-1} h^{-1}) over 7 injections into the GC-MS system under illumination (total irradiation time = 4 h). Prior to Pt deposition on TiO_2/WO_3, the optimum amount of WO_3 was previously evaluated by the photocatalytic experiments. The results have shown that the CO_2 evolution rate was more affected by the materials with higher amounts of WO_3
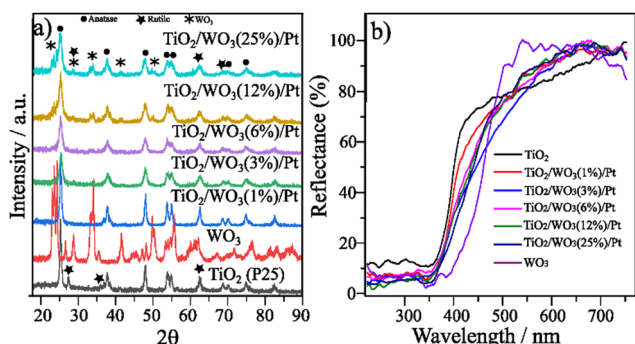

Fig. 1 (a) XRD patterns of TiO_2, WO_3 and $TiO_2/WO_3/Pt$ heterojunction photocatalysts varying their composition and (b) diffuse reflectance spectra of TiO_2, WO_3 and $TiO_2/WO_3/Pt$ photocatalysts varying the concentration of WO_3.
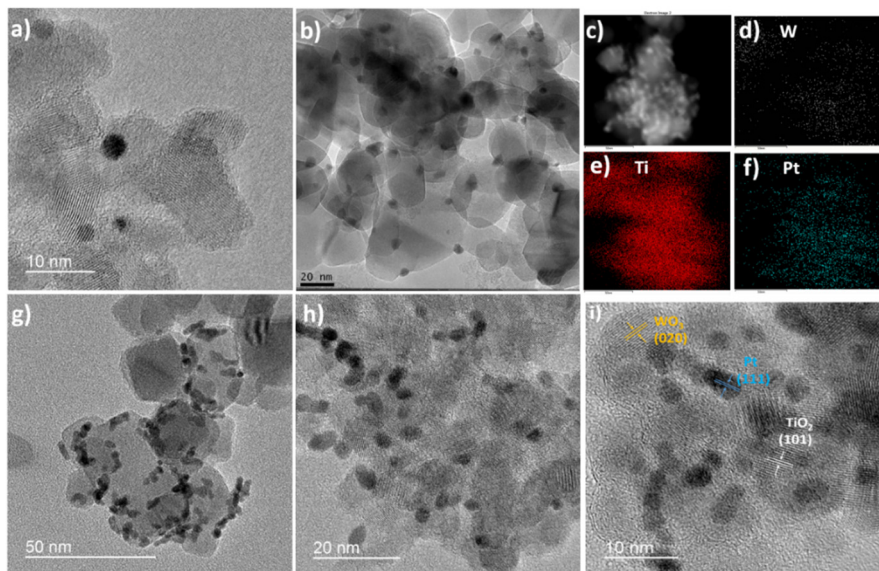
Fig. 2 TEM images of (a) TiO_2/Pt and (b) TiO_2/WO_3 materials; (c) TiO_2/WO_3/Pt (EDX scan image) with its (d) W, (e) Ti and (f) Pt distribution; TEM images of (g)–(i) the TiO_2/WO_3/Pt heterojunction photocatalyst.

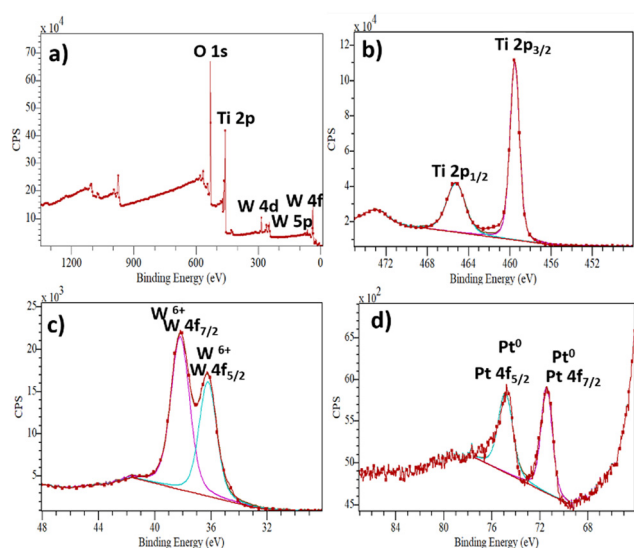**Fig. 3** XPS spectra of the TiO_2/WO_3/Pt photocatalyst: (a) typical survey, (b) Ti 2p, (c) W4f and (d) Pt 4f.

Fig. 4 CH_4 conversion into products over TiO_2, TiO_2/WO_3 and TiO_2/WO_3/Pt photocatalysts towards (a) C_2H_6, (b) CO_2 and (c) H_2 generation. The TiO_2 used as a support was P25 Degussa and the Pt concentration of Pt was set to 0.5%. The time difference between each injection is 33 minutes, corresponding to 4 hours of continuous irradiation.

(12 and 25%), where CO_2 production was decreased by 69% by TiO_2/WO_3(12%) and 49% by TiO_2/WO_3(25%), compared with pristine TiO_2 (P25), as shown in Fig. 4a. The C_2H_6 production was even more affected by higher amounts of WO_3 and it is clearly observed that the production rate decreases constantly from the first to the last injection, reaching values lower than those by pristine TiO_2, suggesting that the WO_3 concentration should be lower. The TiO_2/WO_3 with 1, 3 and 6% of WO_3 generated higher amounts of C_2H_6 with comparable values for CO_2 with pristine P25. As depicted in Fig. 4c, no H_2 evolution was achieved by the pristine TiO_2 and TiO_2/WO_3 photocatalysts.
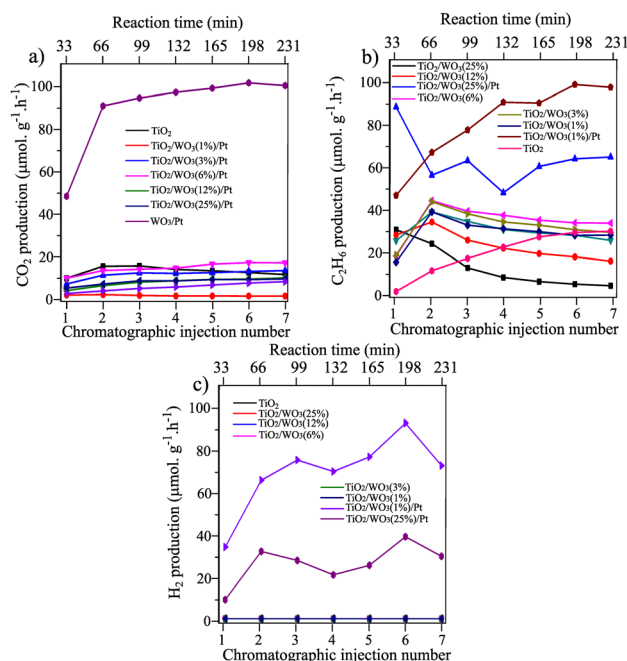
Observing the photocatalytic activity of the materials after Pt loading, the beneficial effect of combining the TiO_2/WO_3 heterostructure with the addition of Pt as a co-catalyst was clearly evidenced. The Pt loading on TiO_2/WO_3(25%) significantly decreased the CO_2 and enhanced the C_2H_6 production, accompanied by H_2 generation. The decrease in CO_2 production

rate was evidence that the undesired overoxidation to CO_2 was inhibited after Pt loading. However, both C_2H_6 and H_2 production did not show stability throughout the reaction, with a rapid decrease in their production within the first three injections, suggesting that the Pt nanoparticles should be incorporated in TiO_2/WO_3 with lower concentration of WO_3.

The rapid decrease in the C_2H_6 and H_2 evolution rate produced by the $TiO_2/WO_3(25\%)/Pt$ photocatalyst within the first three injections (Fig. 4b and c) may be assigned to the possible W^{6+} reduction to W^{5+} by receiving electrons from the conduction band (CB) of TiO_2 upon illumination,[39–41] decreasing their availability to drive the desired chemical reactions. Therefore, the electron transfer from the CB of TiO_2 to the CB of WO_3 with the subsequent reduction process of W^{6+} was competitive with the coupling reactions. This led to a rapid decrease in the C_2H_6 evolution rate accompanied by a photocatalyst colour change from light yellow to dark blue.

After the deposition of Pt nanoparticles on the $TiO_2/WO_3(1\%)$ material, a substantial increase in all products was observed, with better stability over the injections. The increased C_2H_6 production was highly different compared with $TiO_2/WO_3(25\%)/Pt$, with a continuous rise during irradiation. The same behaviour is observed for CO_2 and H_2 production, with a boosted production of both products from the first to the second injection, accompanied by a gradual increase in their production. Considering that the photocatalytic activity of $TiO_2/WO_3/Pt$ heterojunction photocatalysts showed a better performance when the WO_3 concentration is very low, Pt loading was carried out on TiO_2/WO_3 with 0.1% of WO_3 and the results are presented in Fig. 5.
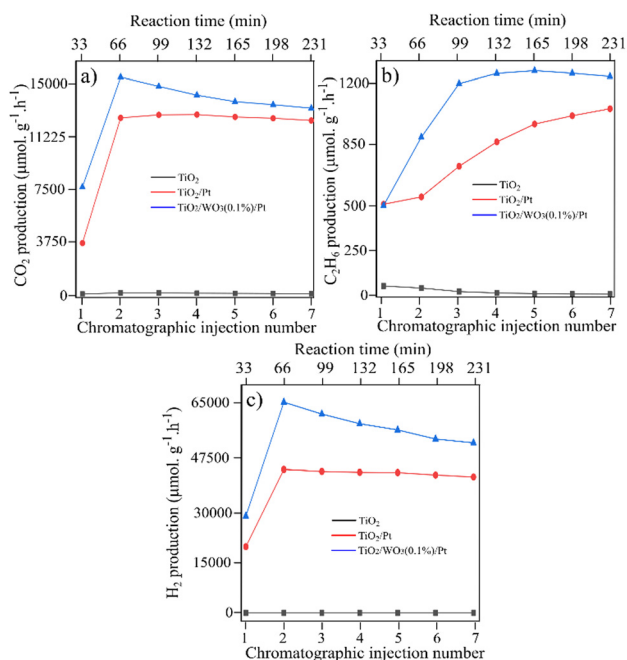

Fig. 5 CH_4 conversion towards the products over TiO_2, TiO_2/WO_3 and $TiO_2/WO_3/Pt$ photocatalysts towards (a) C_2H_6, (b) CO_2 and (c) H_2 generation. The TiO_2 used as support was commercial P25 Degussa.

Fig. 5 shows the photocatalytic activity over pristine TiO_2 (P25), TiO_2/Pt and $TiO_2/WO_3(0.1\%)/Pt$ photocatalysts. Here, both TiO_2/Pt and $TiO_2/WO_3(0.1\%)/Pt$ photocatalysts presented a boosted photoactivity towards CO_2, C_2H_6 and H_2 evolution rate compared with pristine TiO_2 (P25). In Fig. 5a, it is observed that the CO_2 produced by Pt-based photocatalysts was very close, but the C_2H_6 and H_2 production showed a substantial difference. For both the TiO_2/Pt and $TiO_2/WO_3(0.1\%)/Pt$ photocatalysts, a continuous increase in C_2H_6 production is observed, but it is more pronounced for $TiO_2/WO_3(0.1\%)/Pt$, reaching values 2.4 times higher from the first (510 µmol g^{-1} h^{-1}) to the third injection (1196 µmol g^{-1} h^{-1}).

The H_2 evolution rate was dramatically improved by Pt loading on TiO_2/WO_3 with 0.1% of WO_3. From the first to the second injection, the H_2 production rate was increased by 115% and 119% by the TiO_2/Pt (from 20 175 µmol g^{-1} h^{-1} to 43 469 µmol g^{-1} h^{-1}) and $TiO_2/WO_3(0.1\%)/Pt$ (from 29 230 µmol g^{-1} h^{-1} to 64 069 µmol g^{-1} h^{-1}) photocatalysts, respectively. The results suggest that the WO_3 concentration in the ternary composite in a very small content is a key point for boosting both C_2H_6 and H_2 production, while maintaining the same amount of CO_2 and CO evolution. These results indicate that, by decreasing the amount of WO_3, charge carrier recombination is inhibited, and hence the photogenerated electrons become more available to drive the coupling reactions, instead of promoting W^{6+} reduction, with the additional Pt effect on collecting them. In contrast, the over-loading of WO_3 domains clearly produced a decrease of the photocatalytic efficiency.

Different works have also shown a significant improvement in charge transfer between TiO_2 and WO_3, reaching better photocatalytic performances when the WO_3 concentration is less than 1%.[42,43] It has been demonstrated that higher WO_3 content increases the concentration of recombination centers for electron/hole pairs, contributing to lowering the photoactivity of TiO_2–WO_3-based photocatalysts.[44]

Karácsonyi and co-workers[45] showed that significant differences in the photocatalytic performance of the $TiO_2/WO_3/(Pt$ or Au) photocatalysts towards oxalic acid degradation were observed only through the position of the noble metal, if the co-catalyst is deposited on TiO_2 or on WO_3. It was demonstrated that, by changing the WO_3 concentration from 1 to 33%, none of the ternary composites reached H_2 values higher than TiO_2/Pt (without WO_3). In our work, our results indicate that an optimum WO_3 content should be lower than 1% to achieve a beneficial effect towards C_2H_6 and H_2 from CH_4 conversion in the presence of water.

The production rates of the main products (C_2H_6, CO, CO_2 and H_2) generated during the photocatalytic tests are summarized in Table 1. The table also depicts the generation of propane (C_3H_8), but in minor quantity and the selectivity of the products. Comparing TiO_2/Pt with the $TiO_2/WO_3(0.1\%)/Pt$ photocatalyst, it can be observed that similar amounts of CO and CO_2 were achieved. However, the incorporation of 0.1% WO_3 to form the heterojunction system increased the C_2H_6 and H_2 production by 37 and 34%, respectively. This behaviour may be associated with the better charge carrier separation

Table 1 Product formation (average values) using commercial TiO$_2$(P25) as a support and TiO$_2$/WO$_3$ and TiO$_2$/WO$_3$/Pt photocatalysts (75 mg of photocatalyst, 250 mL H$_2$O, 25 mL min^{-1} CH$_4$ (flow rate), 450 W Hg lamp) during methane coupling in the presence of water

Photocatalyst	Product formation rates (µmol g^{-1} h^{-1})					Product selectivity (%)			
	C$_2$H$_6$	C$_3$H$_8$	CO	CO$_2$	H$_2$	C$_2$H$_6$	C$_3$H$_8$	CO	CO$_2$
TiO$_2$ (P25)	45	4.0	46	177	—	16.5	1.5	16.9	65.1
TiO$_2$/WO$_3$ (1%)	60	8.1	30	134	—	25.9	3.5	12.9	57.7
TiO$_2$/WO$_3$ (3%)	66	9.2	36	133	—	27.0	3.8	14.7	54.5
TiO$_2$/WO$_3$ (6%)	69	7.1	29	234	—	20.3	2.1	8.6	69.0
TiO$_2$/WO$_3$ (12%)	11	0.7	40	189	—	4.6	0.3	16.6	78.5
TiO$_2$/WO$_3$ (25%)	23	1.3	6.7	29	—	38.3	2.2	11.2	48.3
TiO$_2$/Pt^a	866	25	20	12 425	42 500	6.5	0.2	0.1	93.2
WO$_3$/Pt^a	5.8	0.6	6.4	29	—	13.9	1.4	15.3	69.4
TiO$_2$/WO$_3$ (0.1%)/Pt^a	1183	33	20	12 745	57 014	8.5	0.2	0.1	91.2
TiO$_2$/WO$_3$ (1%)/Pt^a	158	8.0	12	1446	4814	16.5	1.5	16.9	65.1
TiO$_2$/WO$_3$ (25%)/Pt^a	109	17	19	96	1847	25.9	3.5	12.9	57.7

^{a} The Pt concentration in all photocatalysts was set at 0.5% as the best condition previously tested.

promoted by the interaction between the two semiconductors.[46,47] By receiving electrons from the CB of TiO$_2$ and injecting holes into its valence band (VB), the presence of WO$_3$ in a small content may significantly decrease the charge carrier recombination in both semiconductors,[48] giving holes and electrons more probability to drive the coupling reactions. Additionally, the boosted hydrogen production could only be possible after the presence of Pt nanoparticles. From the viewpoint of selectivity, CO$_2$ is the dominant product generated, reaching 93.2 and 91.2% among the main products produced by TiO$_2$/Pt and TiO$_2$/WO$_3$(0.1%)/Pt photocatalysts, respectively. The higher C$_2$H$_6$ selectivity for TiO$_2$/WO$_3$(0.1%)/Pt (8.5%) compared with TiO$_2$/Pt (6.5%) implies the more efficient formation of $^\bullet$CH$_3$ by the photogenerated holes of WO$_3$.

To further investigate the possible reasons for the enhanced photocatalytic activity of TiO$_2$/WO$_3$(0.1%)/Pt towards C$_2$H$_6$ and H$_2$ evolution, the PL spectra of pristine TiO$_2$ (P25), TiO$_2$/Pt and TiO$_2$/WO$_3$(0.1%)/Pt were evaluated, as shown in Fig. 6. The peak located at 440 nm is mainly originated from the recombination of photogenerated electrons in oxygen vacancies or crystal defects in TiO$_2$.[49] Among the samples, pristine TiO$_2$ (P25) displays the highest PL signal. The TiO$_2$/Pt and TiO$_2$/WO$_3$(0.1%)/Pt reduced the PL intensity by 66 and 83%, respectively, compared to pristine TiO$_2$. The better charge transfer between TiO$_2$ and WO$_3$ can significantly accelerate the carrier separation and suppress the fast recombination of the photoexcited electron–hole pair, which is a key factor in the photocatalytic reaction.[50,51] This evidence together with the results shown in Table 1 clearly demonstrates the synergistic effect of charge separation promoted by WO$_3$ together with the charge transfer promoted by Pt.

More recently, Sato and co-workers[52] have shown that, combining real-time mass spectrometry and operando infrared absorption spectroscopy with *ab initio* molecular dynamics simulations, the C–H bond breaking of CH$_4$ can be effectively enhanced in the presence of water, preventing the overstabilization of the intermediates. In addition, the water-assisted[4] effects contribute to improving the photocatalytic conversion rates at ambient temperatures and pressures. In our work, combining methane conversion in the presence of water using a TiO$_2$/WO$_3$/Pt heterojunction under mild conditions collected
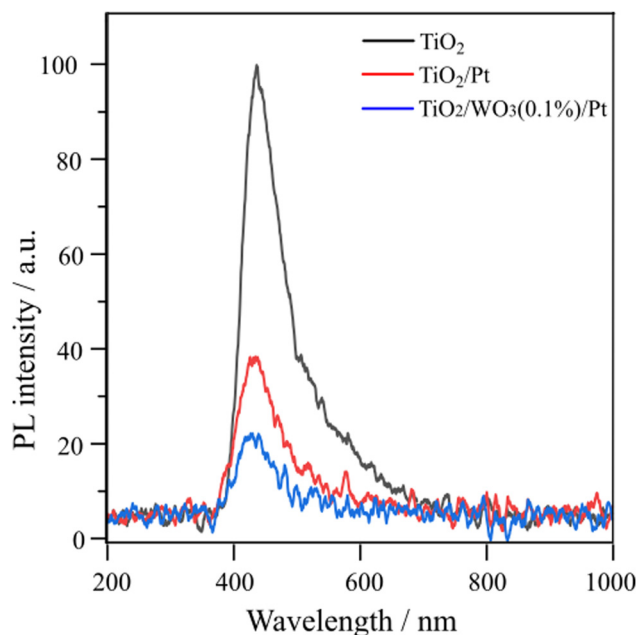

Fig. 6 Room-temperature PL emission spectra of pristine TiO$_2$ (P25), TiO$_2$/Pt and TiO$_2$/WO$_3$/Pt photocatalysts (excitation wavelength at 265 nm).

all the advantages to boost the conversion of CH$_4$ to C$_2$H$_6$ concomitantly with an increase in H$_2$ evolution, although CO$_2$ is still the main product coming from CH$_4$ conversion.

The proper alignment of the energy levels of the VB and CB in TiO$_2$ and WO$_3$ promoting the charge transfer between them is displayed in Fig. 7. Upon illumination, both TiO$_2$ and WO$_3$ semiconductors absorb energy higher than their bandgap values, generating electron/hole pairs. The formation of a TiO$_2$/WO$_3$ heterojunction provides the thermodynamic driving force for the direct electron transfer from the CB of TiO$_2$ into the CB of WO$_3$, whereas holes in the VB of WO$_3$ move to the VB of TiO$_2$, thereby inhibiting deleterious charge carrier recombination.[53] By introducing Pt nanoparticles, efficient cooperation between the charge separation through the heterojunction system and the collection of electrons over Pt sites is achieved.[54]
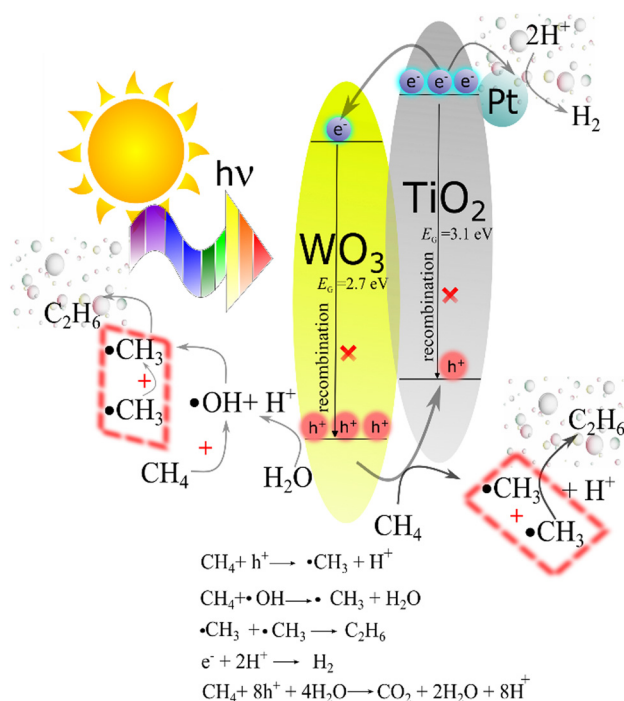
Fig. 7 Energy diagram depicting the charge carrier flux in the $TiO_2/WO_3/Pt$ ternary photocatalyst under illumination, inhibiting charge carrier recombination towards CH_4 conversion and H_2 production.

Fig. 7 also shows the photocatalytic processes of the main products achieved in our system. Firstly, $^{\bullet}CH_3$ radicals are formed from water reacted with h^+. Afterwards, the following coupling of $^{\bullet}CH_3$ is responsible for C_2H_6 production, while electrons (e^-) at the Pt sites reduce H^+ species to form H_2. The overoxidation of CH_4 towards CO_2 is carried out by holes, being the main product of the overall reaction.

Yu and co-workers[55] also describe the role of Pt in promoting the activation of CH_4 molecules to form $^{\bullet}CH_3$ radicals over TiO_2/Pt photocatalysts during direct methane conversion and hydrogen evolution in a photocatalytic system. They show that the subsequent coupling of $^{\bullet}CH_3$ brings up the C_2H_6 product, while H_2 is generated through H^+ reaction with electrons.

In our work, efficient charge carrier separation was obtained through the combination of a TiO_2/WO_3 heterojunction system in cooperation with Pt co-catalysts to promote higher C_2H_6 and H_2 generation. Here, TiO_2/Pt and $TiO_2/WO_3(0.1\%)/Pt$ photocatalysts generated equal values of CO_2, while C_2H_6 and H_2 production presented a substantial improvement, demonstrating the beneficial effect of combining charge carrier transfer through the heterojunction of TiO_2/WO_3 with the additional role of Pt on promoting boosted CH_4 conversion.

Conclusions

Owing to the introduction of WO_3 and Pt, the $TiO_2/WO_3/Pt$ heterojunction photocatalyst exhibited better performance over CH_4 conversion into C_2H_6 and H_2 compared to the pristine materials. Pristine TiO_2 (P25) nanoparticles were proved to be ineffective in driving CH_4 conversion with no H_2 production. This study showed that the presence of WO_3 in a low concentration is an efficient way to benefit the C_2H_6 formation rate due to better charge separation and by introducing Pt nanoparticles, H_2 generation was achieved. The synergistic effect between the materials contributed to the selective coupling of CH_4 towards C_2H_6 and H_2 production. Herein, we described the achievement of a new promising candidate material towards methane conversion with simultaneous generation of hydrogen through a non-thermal heterogeneous catalysis of methane under mild conditions. Notwithstanding this, CO_2 remains the primary product generated from methane. The pursuit of enhancing photocatalyst activity and refining selectivity toward the desired products remains an ongoing imperative. This work may be helpful for extending the possibilities towards the design of future nanomaterials for methane coupling with hydrogen generation in the presence of water simultaneously in one system.

Author contributions

Conflicts of interest

There are no conflicts to declare.

Acknowledgements

References

1 M. Z. Jacobson, *Energy Environ. Sci.*, 2009, **2**, 148–173.
2 J. R. McKone, D. C. Crans, C. Martin, J. Turner, A. R. Duggal and H. B. Gray, *Inorg. Chem.*, 2016, **55**, 9131–9143.

3   T. Shi, D. Sridhar, L. Zeng and A. Chen, *Electrochem. Commun.*, 2022, **135**, 107220.

4   H. Sato, A. Ishikawa, H. Saito, T. Higashi, K. Takeyasu and T. Sugimoto, *Commun. Chem.*, 2023, **6**, 8.

5   J. Zhao, H. Yan and J. Zeng, *Chem Catal.*, 2022, **2**, 1521–1523.

6   M. Ishimaru, F. Amano, C. Akamoto and S. Yamazoe, *J. Catal.*, 2021, **397**, 192–200.

7   Y. Tang, Y. Li and F. (Feng) Tao, *Chem. Soc. Rev.*, 2022, **51**, 376–423.

8   S. Wu, X. Tan, J. Lei, H. Chen, L. Wang and J. Zhang, *J. Am. Chem. Soc.*, 2019, **141**, 6592–6600.

9   F. He, F. Ma, T. Li and G. Li, *Chin. J. Catal.*, 2013, **34**, 2263–2270.

10 J. A. Pinedo-Escobar, J. Fan, E. Moctezuma, C. Gomez-Solís, C. J. Carrillo Martinez and E. Gracia-Espino, *ACS Omega*, 2021, **6**, 11840–11848.

11 S. Wu, L. Wang and J. Zhang, *J. Photochem. Photobiol., C*, 2021, **46**, 100400.

12 L. Yu and D. Li, *Catal. Sci. Technol.*, 2017, **7**, 635–640.

13 M. Ishimaru, F. Amano, C. Akamoto and S. Yamazoe, *J. Catal.*, 2021, **397**, 192–200.

14 Y. Liu, Y. Chen, W. Jiang, T. Kong, P. H. C. Camargo, C. Gao and Y. Xiong, *Research*, 2022, **2022**, 9831340.

15 H. Song, X. Meng, S. Wang, W. Zhou, S. Song, T. Kako and J. Ye, *ACS Catal.*, 2020, **10**, 14318–14326.

16 K. Dutta, M. Shahryari and J. Kopyscinski, *Ind. Eng. Chem. Res.*, 2020, **59**, 4245–4256.

17 L. Li, S. Fan, X. Mu, Z. Mi and C.-J. Li, *J. Am. Chem. Soc.*, 2014, **136**, 7793–7796.

18 S. P. Singh, A. Anzai, S. Kawaharasaki, A. Yamamoto and H. Yoshida, *Catal. Today*, 2021, **375**, 264–272.

19 E. R. Januario, S. A. Carminati, A. Tofanello, B. L. da Silva, P. F. Silvaino, A. P. Machado, J. M. Vaz and E. V. Spinacé, *Sustainable Energy Fuels*, 2023, **7**, 4288–4296.

20 S. Murcia-López, K. Villa, T. Andreu and J. R. Morante, *Chem. Commun.*, 2015, **51**, 7249–7252.

21 A. P. Machado, S. A. Carminati, E. R. Januário, P. S. Ferreira, J. M. Vaz and E. V. Spinacé, *Methane*, 2023, **2**, 44–55.

22 S. J. Armaković, M. M. Savanović and S. Armaković, *Catalysts*, 2022, **13**, 26.

23 W. Zhang, C. Fu, J. Low, D. Duan, J. Ma, W. Jiang, Y. Chen, H. Liu, Z. Qi, R. Long, Y. Yao, X. Li, H. Zhang, Z. Liu, J. Yang, Z. Zou and Y. Xiong, *Nat. Commun.*, 2022, **13**, 2806.

24 D. R. Aireddy, A. Roy, D. A. Cullen and K. Ding, *Catal. Today*, 2023, **416**, 113977.

25 Z. Liu, B. Xu, Y.-J. Jiang, Y. Zhou, X. Sun, Y. Wang and W. Zhu, *ACS Environ. Au*, 2023, **3**(5), 252–276.

26 G. Yuniar, W. H. Saputera, D. Sasongko, R. R. Mukti, J. Rizkiana and H. Devianto, *Molecules*, 2022, **27**, 5496.

27 Y. Wang, H. Fu, X. Yang, X. An, Q. Zou, S. Xiong and D. Han, *J. Mater. Sci.*, 2020, **55**, 14415–14430.

28 K. Kighuta, A.-I. Gopalan, D.-G. Lee, S.-W. Kim, S.-S. Park, D.-E. Lee, K.-P. Lee and W.-J. Kim, *J. Environ. Chem. Eng.*, 2022, **10**, 108224.

29 J. Yang, D. Wang, H. Han and C. Li, *Acc. Chem. Res.*, 2013, **46**, 1900–1909.

30 M. Kang, J. Liang, F. Wang, X. Chen, Y. Lu and J. Zhang, *Mater. Res. Bull.*, 2020, **121**, 110614.

31 H. Yaghoubi, Z. Li, Y. Chen, H. T. Ngo, V. R. Bhethanabotla, B. Joseph, S. Ma, R. Schlaf and A. Takshi, *ACS Catal.*, 2015, **5**, 327–335.

32 D. Cani, J. C. van der Waal and P. P. Pescarmona, *Appl. Catal., A*, 2021, **621**, 118179.

33 F. Raziq, A. Aligayev, H. Shen, S. Ali, R. Shah, S. Ali, S. H. Bakhtiar, A. Ali, N. Zarshad, A. Zada, X. Xia, X. Zu, M. Khan, X. Wu, Q. Kong, C. Liu and L. Qiao, *Adv. Sci.*, 2022, **9**, 2102530.

34 M. Zych, K. Syrek, L. Zaraska and G. D. Sulka, *Molecules*, 2020, **25**, 2916.

35 Y. Wang, H. Fu, X. Yang, X. An, Q. Zou, S. Xiong and D. Han, *J. Mater. Sci.*, 2020, **55**, 14415–14430.

36 N. Kunthakudee, T. Puangpetch, P. Ramakul and M. Hunsom, *ACS Omega*, 2022, **7**(9), 7683–7695.

37 B. Gong, X. Luo, N. Bao, J. Ding, S. Li and J. Yi, *Surf. Interface Anal.*, 2014, **46**, 1043–1046.

38 Y. Wang, H. Fu, X. Yang, X. An, Q. Zou, S. Xiong and D. Han, *J. Mater. Sci.*, 2020, **55**, 14415–14430.

39 L. Zhang, M. Qin, W. Yu, Q. Zhang, H. Xie, Z. Sun, Q. Shao, X. Guo, L. Hao, Y. Zheng and Z. Guo, *J. Electrochem. Soc.*, 2017, **164**, H1086–H1090.

40 N. M. Makwana, R. Quesada-Cabrera, I. P. Parkin, P. F. McMillan, A. Mills and J. A. Darr, *J. Mater. Chem. A*, 2014, **2**, 17602–17608.

41 A. Habtamu and M. Ujihara, *RSC Adv.*, 2023, **13**, 12926–12940.

42 J. Lee and W.-K. Jo, *Catalysts*, 2017, **7**, 97.

43 M. V. Dozzi, S. Marzorati, M. Longhi, M. Coduri, L. Artiglia and E. Selli, *Appl. Catal., B*, 2016, **186**, 157–165.

44 B. Grbić, N. Radić, S. Stojadinović, R. Vasilić, Z. Dohčević-Mitrović, Z. Šaponjić and P. Stefanov, *Surf. Coat. Technol.*, 2014, **258**, 763–771.

45 É. Karácsonyi, L. Baia, A. Dombi, V. Danciu, K. Mogyorósi, L. C. Pop, G. Kovács, V. Coşoveanu, A. Vulpoi, S. Simon and Z. Pap, *Catal. Today*, 2013, **208**, 19–27.

46 I. A. Castro, G. Byzynski, M. Dawson and C. Ribeiro, *J. Photochem. Photobiol., A*, 2017, **339**, 95–102.

47 L. Zhang, J. Guo, B. Hao and H. Ma, *Opt. Mater.*, 2022, **133**, 113035.

48 N. Moghni, H. Boutoumi, H. Khalaf, N. Makaoui and G. Colón, *J. Photochem. Photobiol., A*, 2022, **428**, 113848.

49 X. Fan, J. Wan, E. Liu, L. Sun, Y. Hu, H. Li, X. Hu and J. Fan, *Ceram. Int.*, 2015, **41**, 5107–5116.

50 I. A. Castro, G. Byzynski, M. Dawson and C. Ribeiro, *J. Photochem. Photobiol., A*, 2017, **339**, 95–102.

51 F. M. Pesci, G. Wang, D. R. Klug, Y. Li and A. J. Cowan, *J. Phys. Chem. C*, 2013, **117**, 25837–25844.

52 H. Sato, A. Ishikawa, H. Saito, T. Higashi, K. Takeyasu and T. Sugimoto, *Commun. Chem.*, 2023, **6**, 8.

53 F. Pinto, A. Wilson, B. Moss and A. Kafizas, *J. Phys. Chem. C*, 2022, **126**, 871–884.

54 H. Gao, P. Zhang, J. Hu, J. Pan, J. Fan and G. Shao, *Appl. Surf. Sci.*, 2017, **391**, 211–217.

55 L. Yu, Y. Shao and D. Li, *Appl. Catal., B*, 2017, **204**, 216–223.